Rakenteiden Mekaniikka (Journal of Structural Mechanics)
Vol. 59, No. 1, 2026, pp. 40–55
https://rakenteidenmekaniikka.journal.fi/index
https://doi.org/10.23998/rm.161988

VERTAISARVIOITU
KOLLEGIALT GRANSKAD
PEER-REVIEWED
www.tsv.fi/tunnus

Comparison of experimental and numerical analysis response in the case of deflection sensor

Mikko Salo[1], Jarno Jokinen, Nazanin Pournoori, Matti Vilkko and Mikko Kanerva

Summary In this study, the data from a sensor for generating and measuring a plate's surface deflection was compared against the data from simulations with the finite element method. The sensor deformed the plate by using a vacuum pressure. The deflection was measured by utilizing photometric stereo techniques with data from an RGB-camera. A finite element model consisting of the relevant parts of the sensor and a volume element model of the plate under a load equivalent to the vacuum pressure of the sensor was used. The material constants of the real plate were approximated by using digital image correlation and applied to the finite element model. The measured deflections and their numerical partial derivatives were compared to their simulated counterparts. The sensitivity of the sensor between multiple images was studied against small changes in simulated deflections when the material constants were varied.

Keywords: photometric stereo, plate, deflection, digital image correlation, finite element method

Received: 26 May 2025. Accepted: 23 March 2026.

Introduction

Measuring mechanical properties of paperboard online during manufacturing is difficult and highly sought after by the paper industry [2, 4, 6, 7]. Accurate online stiffness measurements would allow manufacturers to better control product quality in real time, reducing waste and improving process efficiency. A novel method for measuring the bending stiffness of paperboard from optical measurements of an induced deflection using analytical plate equations was proposed in [8]. The method suffered from noisy data and was later tested using a finite element (FE) model of the practical measurement setup [9, 10]. Such models are generally used to simulate the behavior of materials and objects under varying loading scenarios, for example when designing a bridge.

The FE simulations showed that the previously proposed method can accurately measure the bending stiffness from simulated deflection data, which is practically noise-free compared to the optical measurements.

This paper studies the accuracy of the FE model compared to the practical optical measurement. The deflection of an isotropic elastic polyethylene (PE, later referred to as plastic) sheet was measured using the optical sensors. The elastic constants, namely

---

[1] Corresponding author: `mikko.salo@tuni.fi`

the elastic modulus and the Poisson's ratio of the plastic were measured using digital image correlation (DIC). The FE model of the measurement setup was simulated using the measured elastic constants of the plastic. The simulated deflections and their partial derivatives were compared to the ones obtained by the optical measurement. A sensitivity analysis of the optical measurement was also conducted, focusing on the level of noise in the measured data in relation to small changes in the material constants in the FE model.

This paper introduces the optical measurement for obtaining real-life deflection data. The DIC measurement of elastic constants and its results are discussed in detail. The FE model of the practical measurement is defined. Finally, the experiments are explained and their results compared and discussed.

Methods

This Section introduces the methods used in this study. Photometric stereo methods are used to record real-life deflection of a plastic sheet under transverse loading. Digital image correlation is then used to record the elastic constants of said plastic sheet. Finally, using these elastic constants and the geometry of the real-life measurement setup, a finite element model is used to simulate deflection data comparable to the one measured with photometric stereo.

Surface deflection from single-image RGB photometric stereo

The sensor for generating and measuring surface deflection comprises of a metal support with a circular cut hole (diameter 23 mm). A measurable and controllable vacuum deforms an elastic plastic sheet residing over the support and the hole. An RGB-camera and sets of directed red, green and blue LED lights are placed on the other side of the plate. The lights illuminate the plate while the camera captures the reflected light intensities. The captured intensities are called an image. The sensors are depicted in Figure 1.

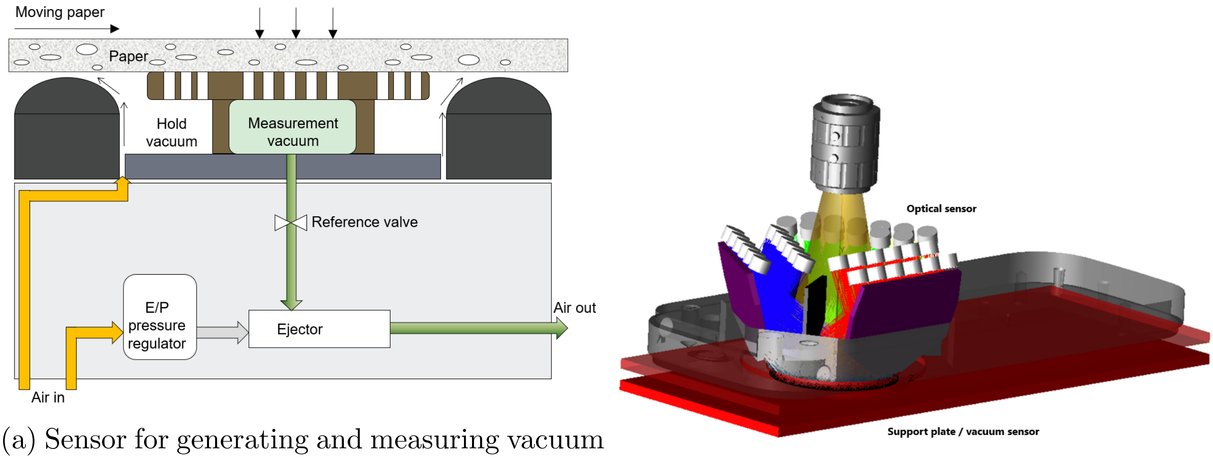

(a) Sensor for generating and measuring vacuum pressure.

(b) Optical sensor for detecting surface shape.

Figure 1: The measurement hardware.

Reference images, taken of a flat surface of the plate, are used to calibrate the lighting, reflectance and camera parameters. The reference surface is assumed perpendicular to the camera direction, meaning that the surface normal points towards the camera. Measurement images are taken of a deformed plate's surface and provide information of the surface shape.

We assume that the light reflection, ρ, is Lambertian and that the surface reflectance is constant. The incident light direction is considered constant within the illuminated area for each color light source. The reflected light intensity of the measurement image is then [1]

$$I = \rho I_0 \langle L, n \rangle, \tag{1}$$

where I_0 is the incident light intensity, L is vector pointing from the surface to the incident light source and n is the surface normal.

If the plate's deflection is small relative to the flat reference surface, we have (noting properties related to the reference image with superscript "r")

$$\begin{aligned} L^r &= L, \\ I_0^r &= I_0, \\ n^r &= \begin{bmatrix} 0 & 0 & 1 \end{bmatrix}^\intercal . \end{aligned} \tag{2}$$

This is to say, that the changes in incident light direction and intensity are negligibly small due to the relatively small changes in the locations of the corresponding surface points between measurement and reference arrangements.

The reference calibration is then done by dividing the recorded intensity values of the measurement image with the reference image:

$$F := \frac{I}{I^r} = \frac{I_0 \langle L, n \rangle}{I_0^r \langle L^r, n^r \rangle} = \frac{\langle L, n \rangle}{\langle L, n^r \rangle} = \frac{\langle L, n \rangle}{L_z}. \tag{3}$$

Applying equation (3) to all channels of the RGB-camera, we have [3]

$$\mathcal{F} = \mathcal{L} n, \tag{4}$$

where

$$\mathcal{F} = \begin{bmatrix} F^R & F^G & F^B \end{bmatrix}^\top \tag{5}$$

is given by the reference calibrated image data and

$$\mathcal{L} = \begin{bmatrix} \frac{1}{L_z^R} & 0 & 0 \\ 0 & \frac{1}{L_z^G} & 0 \\ 0 & 0 & \frac{1}{L_z^B} \end{bmatrix} \begin{bmatrix} L_x^R & L_y^R & L_z^R \\ L_x^G & L_y^G & L_z^G \\ L_x^B & L_y^B & L_z^B \end{bmatrix} \tag{6}$$

comes from the system geometry, namely the light source directions L.

The surface normals are then solved from

$$n = \frac{(\mathcal{L}^\top \mathcal{L})^{-1} \mathcal{L}^\top \mathcal{F}}{||(\mathcal{L}^\top \mathcal{L})^{-1} \mathcal{L}^\top \mathcal{F}||}, \tag{7}$$

assuming $\mathcal{L}$ has full rank. Finally, the first partial derivatives of the parametrized surface height profile $Z(x, y)$ are given by

$$\frac{\partial Z}{\partial x} = -\frac{n_x}{n_z}, \quad \frac{\partial Z}{\partial y} = -\frac{n_y}{n_z}. \tag{8}$$

The following formulation approximates the surface from its measured partial derivatives according to Frankot and Chellappa [5]. The formulation is an adaptation for use with Matlab *fft2* and *ifft2* functions. For an image of size $N \times N$ pixels, let

$$Z_{p,q} := Z(x_p, x_q), \quad p, q \in \{1, \dots, N\} \tag{9}$$

describe the data at point (x_p, x_q). The surface data Z is then approximated by $\tilde{Z}$ using discrete Fourier basis functions:

$$\tilde{Z}_{p,q} = \frac{1}{N^2} \sum_{j,k=1}^{N} \tilde{C}_{j,k} \omega^{-(j-1)p} \omega^{-(k-1)q}, \tag{10}$$

where

$$\omega = \exp\left(- \frac{i2\pi}{N} \right) \tag{11}$$

and i is the imaginary unit. Let

$$\begin{aligned} C^x_{j,k} &= \sum_{p,q=1}^{N} \frac{\partial Z_{p,q}}{\partial x} \omega^{(j-1)p} \omega^{(k-1)q}, \\ C^y_{j,k} &= \sum_{p,q=1}^{N} \frac{\partial Z_{p,q}}{\partial y} \omega^{(j-1)p} \omega^{(k-1)q}, \quad j, k \in \{1, \dots, N\} \end{aligned} \tag{12}$$

denote the optimal Fourier coefficients of the x- and y-partial derivatives 8. The optimal Fourier coefficients of the surface approximation $\tilde{Z}_{p,q}$ are then given by the integration

$$\tilde{C}_{j,k} = -\frac{i}{2\pi} \frac{\Delta_d \left(u_j C^x_{j,k} + u_k C^y_{j,k} \right)}{u_j^2 + u_k^2}, \tag{13}$$

where [2]

$$u = \frac{1}{N} \left[0, \dots, \mathrm{floor}\left(\frac{N-1}{2} \right), -\mathrm{ceil}\left(\frac{N-1}{2} \right), \dots, -1 \right] \tag{14}$$

and

$$\Delta_d = x_{p+1} - x_p \tag{15}$$

is the data box length (pixel size). The integration constant $\tilde{C}_{1,1}$ is set to 0 since it is not known.

DIC measurement of material constants

Tensile characterization of plastic sheets was carried out using optical imaging with digital image correlation (DIC) to measure the elastic modulus and Poisson's ratio. Quasi-static uniaxial tensile tests were performed with Instron 5967 universal testing machine equipped with a 500 N load cell. Thin plastic sheets (thickness ∼ 0.5 mm) were cut into rectangular strips with dimensions of 100×10 mm^2. Before testing, the test strips were prepared with a very fine layer of black speckle pattern for DIC measurements. All tests were conducted

---

[2] This is *ifftshift*$\left(\frac{1}{N} \left[-\mathrm{ceil}\left(\frac{N-1}{2}\right), \dots, \mathrm{floor}\left(\frac{N-1}{2}\right) \right] \right)$ in Matlab.

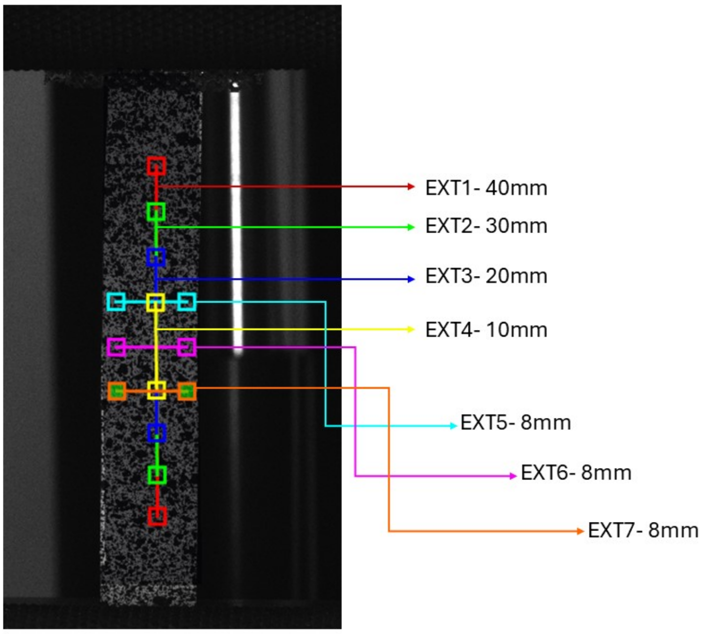

Figure 2: The digital extensometers used to calculate the strain in the DIC tests.

at a constant cross-head displacement rate of 10 mm/min at room temperature (21±2 °C) and 50 ± 5 % relative humidity. The quasi-static tests were imaged using two M-Lite 16 Mpix CMOS cameras with Nikon AF Micro-Nikkor 100 mm f/4D IF-ED lenses at an acquisition rate of 1 Hz. The optical cameras were connected with the ADC converter to the testing machine for synchronizing the force data and the recorded deformation. The optical image resolution was 1578 × 3150 pixels with a pixel size of 30 μm/pixel and an exposure time of 15 μs.

The full-field displacements and strains were calculated using Stereo-DIC with the commercial package DAVIS 11 (LaVision, Göttingen, Germany). The optical images were correlated with the Sum-of-differential using subset size of 55 × 55 pixels^2 and step size of 18 pixels. The matching process of the DIC analysis was performed using a quadratic shape function and a 6th order B-Spline interpolation scheme with the zero-normalized sum of squared differences (ZNSSD) criterion.

The full-field strains were obtained using various virtual extensometers placed on the part of the strip surface vertically and horizontally, as shown in Figure 2. Therefore, the engineering strains were determined both in the longitudinal and transverse directions, which enabled the calculation of Poisson's ratios. Figure 3 shows the stress-strain curves of the tested strips, where the strains obtained using virtual extensometers in the longitudinal direction, EXT1-EXT3. The elastic modulus of the material strip was determined by using the slope of the engineering stress-strain curve. For this purpose, a first-degree polynomial (least squares fit) regression was used to obtain the slope of the linear-elastic region of the curves. The linear regime was estimated for the strain values between 0.001 and 0.008 mm/mm. Poisson's ratio of the material was determined from the virtual vertical and horizontal extensometers, EXT3 and EXT6, respectively. The results are shown in Figure 4

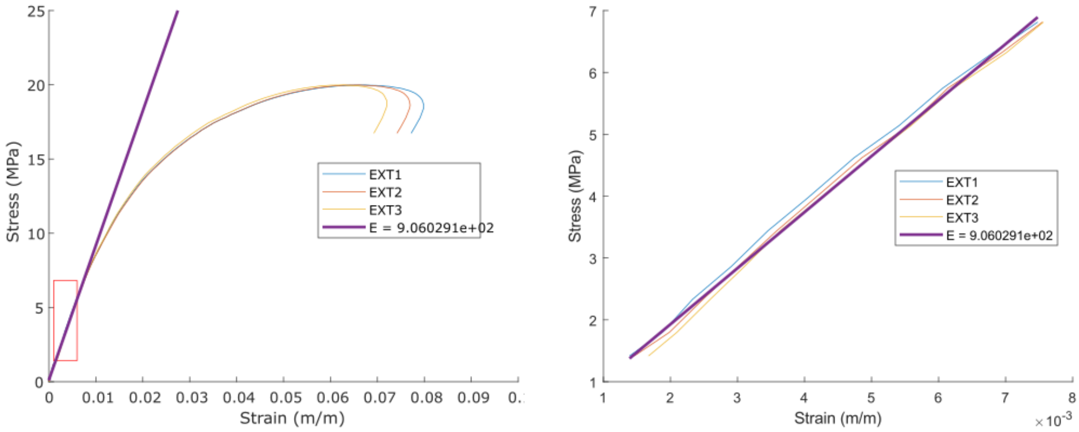

(a) The measured stress-strain curves and the linear least squares fit.

(b) The figure zoomed to the region of the least squares fit.

Figure 3: The DIC-measured stress-strain curves for different extensometers and the calculated elastic modulus.

Finite element model

A FE model of the relevant parts of the measurement system was created in Abaqus/Standard 2021 (Simulia). The model of the sensor for generating the vacuum pressure is a rectangular support plate with a circular 23 mm (diameter) hole in the middle. The edges of the hole are chamfered with a 0.4 mm radius. The model of the plastic sheet, resting initially on top of the rigid plate, is 52 mm ×52 mm wide and 0.522 mm thick plate. The model is illustrated in Figure 5.

The plastic sheet was modelled as an isotropic solid 3D-object. The elastic modulus and Poisson's ratio were measured 920 MPa and 0.36, respectively, from real plastic sheet. The support is an isotropic homogeneous solid, analytically rigid 3D-object. The rigid body motion of the support was restricted in all directions. No boundary conditions were given to the plastic sheet.

The plastic sheet model is meshed with 0.261 mm cubic elements, totaling 200 elements in the width directions and two elements in the thickness direction. A mesh resulting in four elements in the thickness direction was also tested, but the difference in the desired properties (namely, the deflection of the mid-surface and its derivatives) was negligible. Uniform shape elements were used so that data differentiation is easier in post-processing. The elements are 3D-stress elements with linear geometric order and reduced integration (C3D8R). The support's less dense mesh consists of linear tetrahedrons (C3D4) that conform better to the chamfered edge of the hole.

To simulate the vacuum pressure difference of the real measurement system, a uniform pressure was set to act on the nodes in the area of the hole in the support plate. The magnitude of the pressure was set to 11.3 kPa, as was measured in the tests with the real system. The contact with the plastic sheet and the support plate was modeled as surface-to-surface with node to surface discretization method. Since the real contact model was not known, frictionless finite sliding formulation was used. The analysis included geometric nonlinearity.

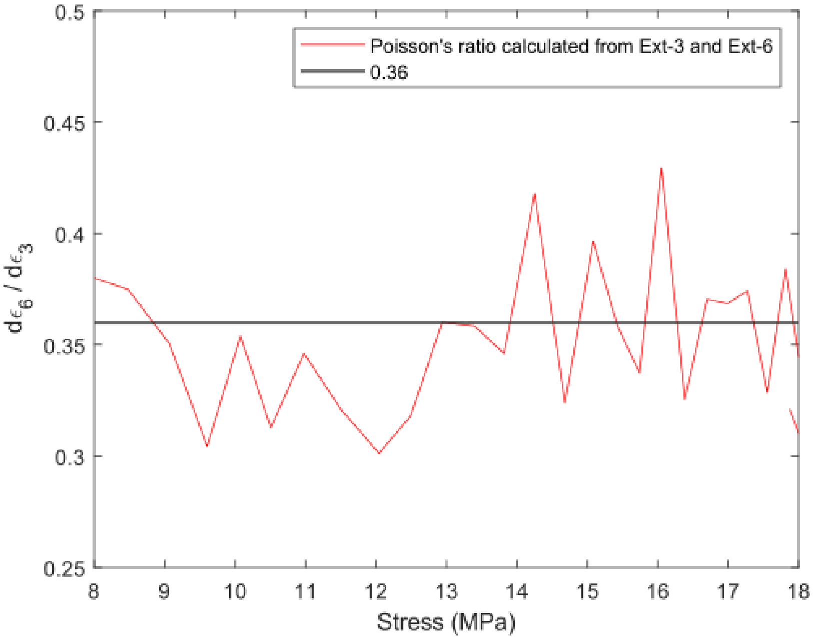

Figure 4: The Poissons ratio determined from extensometers 3 and 6 as a function of the stress in DIC test.

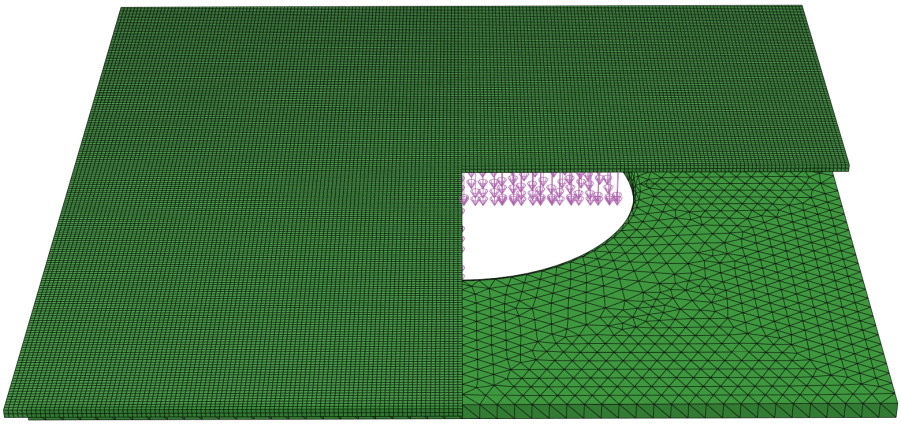

Figure 5: An illustration of the finite element model.

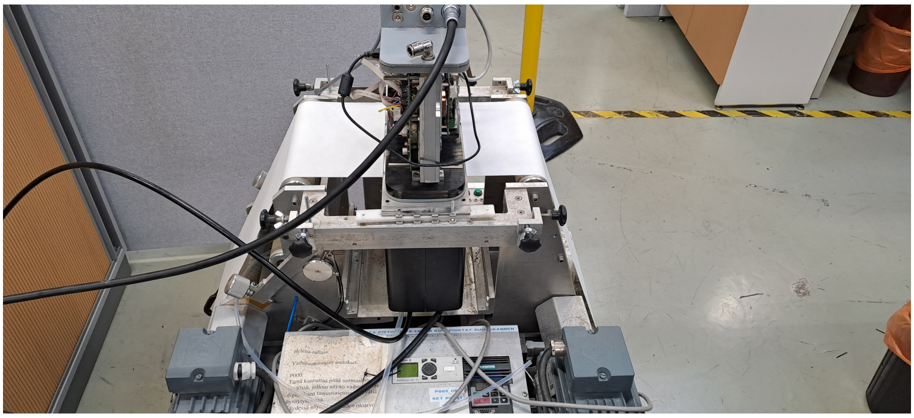

Figure 6: The setup of the optical measurement.

Experiments

Comparison of optical surface deflection measurements with FE-simulated ones

The deflection of the plastic sheet was measured with the optical measurement system and compared to that simulated by the FE model. In addition, the deflections were numerically differentiated using central difference formula and some partial derivatives were compared.

The practical measurement was conducted on a relatively wide and long (compared to the measurement area) plastic sheet was placed in the sensor, resting between two idle rollers. The other end of the strip was clamped far from the measurement area. A slight tension was introduced to the other end, also very far from the measurement area, in order to pull away any slack to obtain a planar reference image measurement for calibration. The test setup is depicted in Figure 6. The vacuum pressure was then applied and measured at 11.3 kPa while capturing a measurement image of size 1392×1392 pixels. The metric size of the image area was recorded at 28 mm. The surface deflection $\tilde{Z}$ was then calculated according to the photometric stereo methods described.

The FE-model was also simulated and the resulting unique nodal out of plane deflections were recorded. There was no significant difference between the deflections of the middle, top or bottom layers of nodes. The maximum stress occurring in the simulation, in the middle of the bottom layer of nodes, was recorded at 2.69 Mpa, which is less than the stress that caused plastic deformations in the DIC tests.

The out of plane deflections recorded by the optical measurement system and the ones simulated by the FE-model were scaled, shifted and magnified to same scale (in meters) and compared. The deflections were also differentiated and the partial derivatives compared. Both measured and simulated partial derivatives were low-pass filtered with the same parameters in order to reduce the compounding noise occurring especially in the case of the measurement. The comparison of the deflections and their partial derivatives is depicted in Figures 7–10.

The effect of edge chamfering was also studied in three different scenarios using the same FE model with different radii for the chamfer in the edge of the hole. The chamfer cases were: no chamfering (sharp 90 degree edge), a chamfer with a radius of 0.4 mm (default case) and a chamfer with a radius of 0.6 mm. A cross-section of the resulting FE-simulated deflections and their first partial derivatives, as well as the measured one, are depicted in Figure 11.

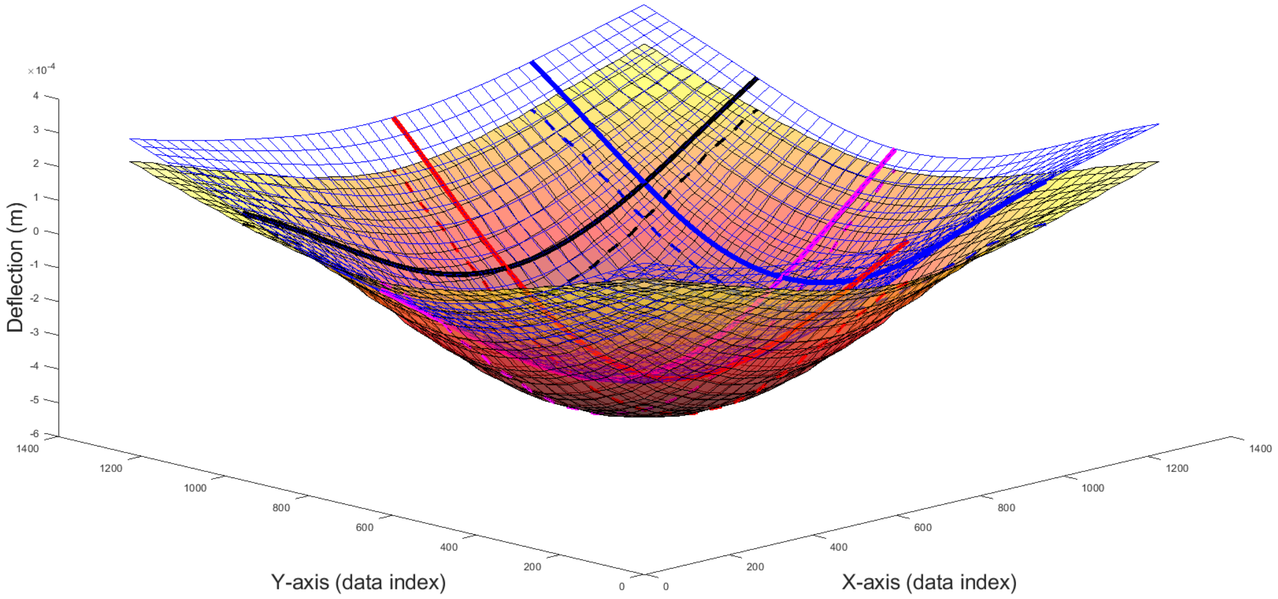

(a) Comparison in 3D. Blue mesh: measured, yellow/red: FEM.

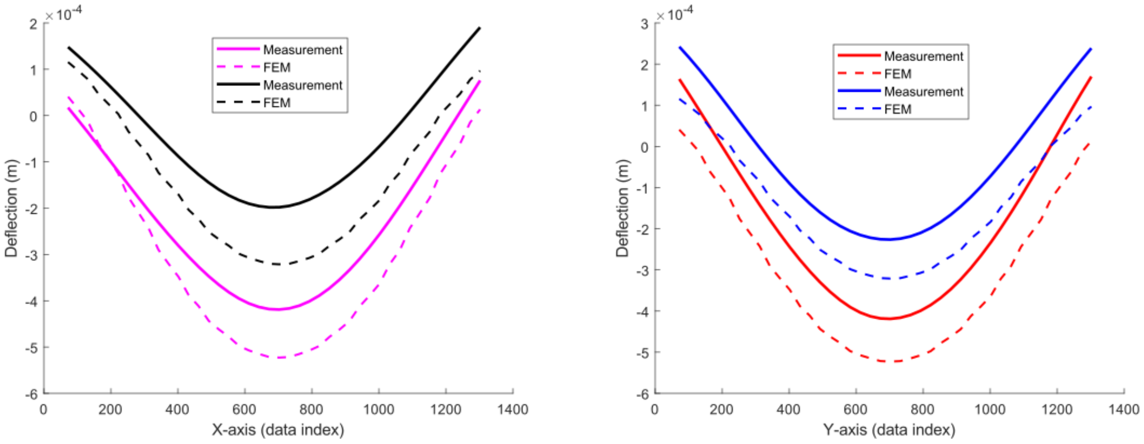

(b) Comparison in X-direction across the depicted lines.

(c) Comparison in Y-direction across the depicted lines.

Figure 7: Comparison of measured and FE-simulated deflections.

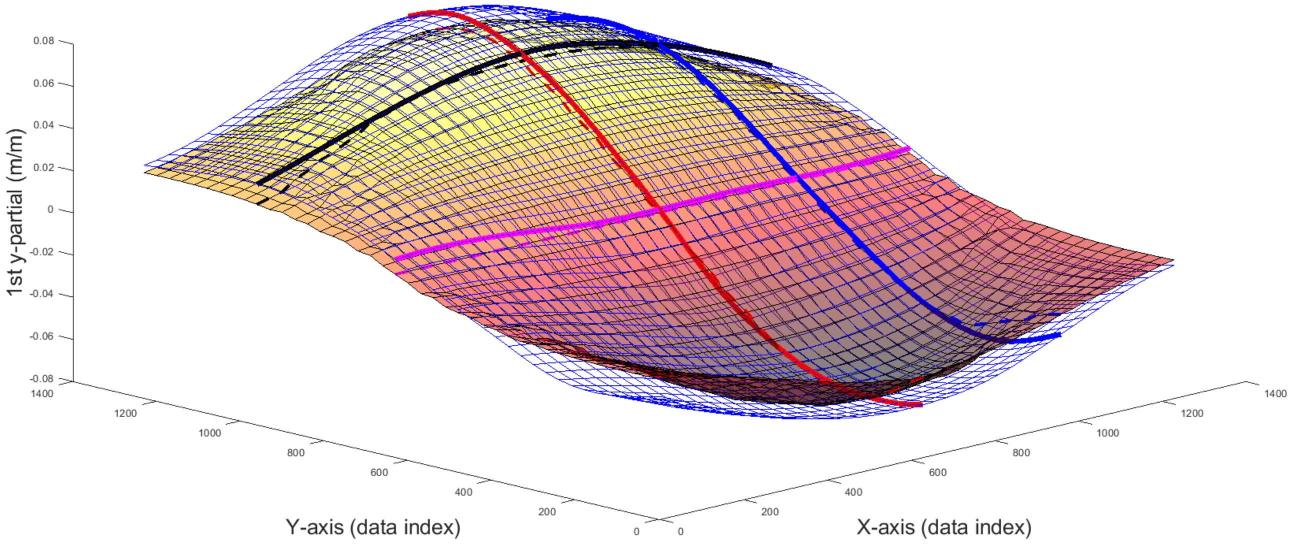

(a) Comparison in 3D. Blue mesh: measured, yellow/red: FEM.

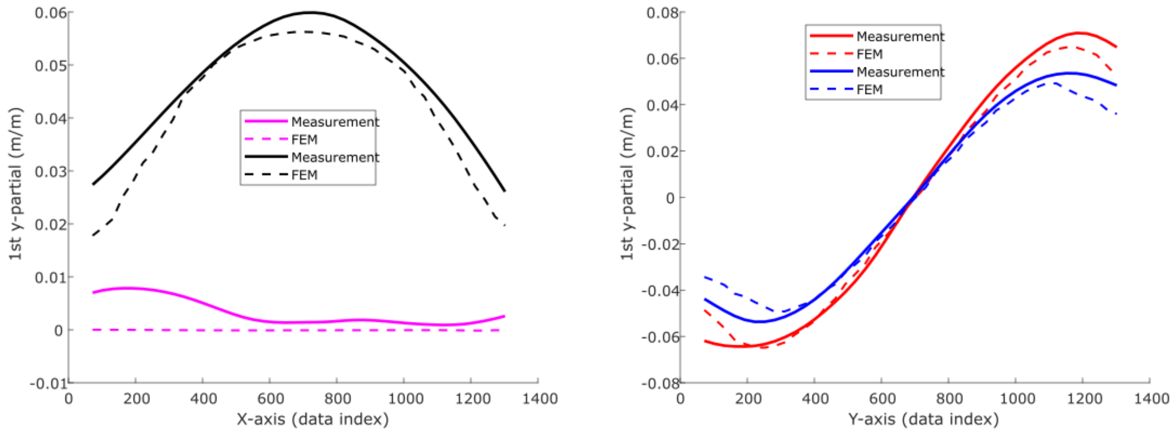

(b) Comparison in X-direction across the depicted lines.

(c) Comparison in Y-direction across the depicted lines.

Figure 8: Comparison of measured and FE-simulated deflections' 1st partial derivatives in y-direction.

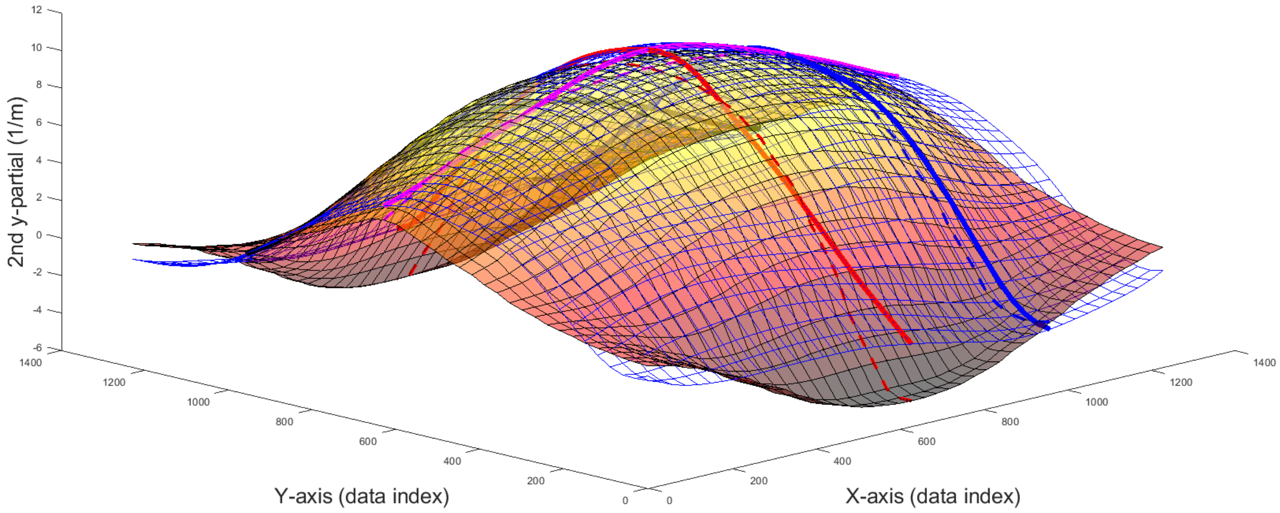

(a) Comparison in 3D. Blue mesh: measured, yellow/red: FEM.

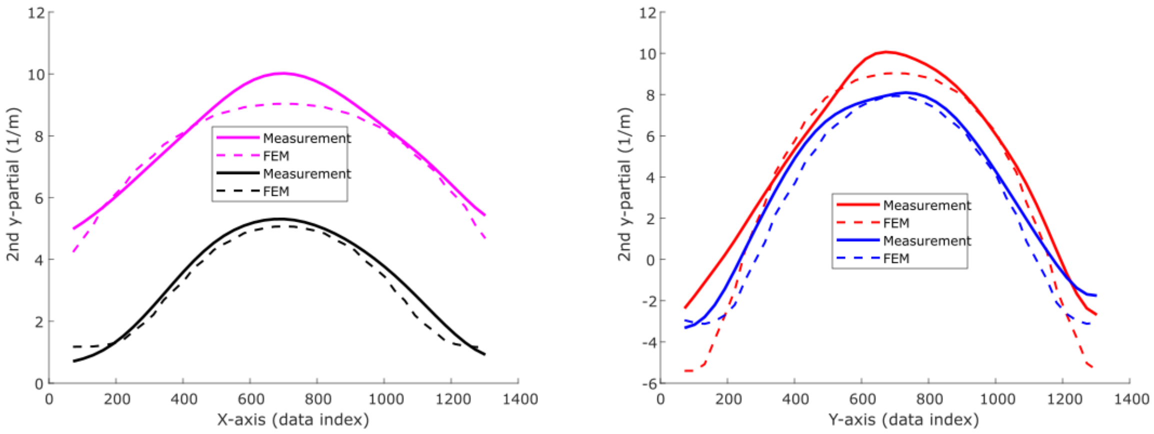

(b) Comparison in X-direction across the depicted lines.

(c) Comparison in Y-direction across the depicted lines.

Figure 9: Comparison of measured and FE-simulated deflections' 2nd partial derivatives in y-direction.

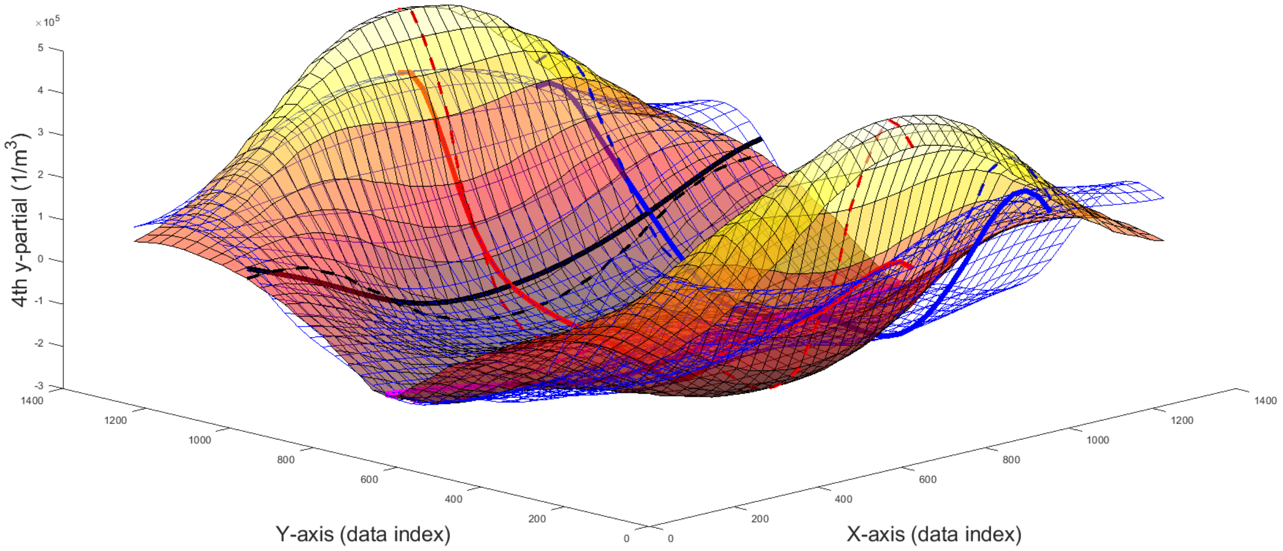

(a) Comparison in 3D. Blue mesh: measured, yellow/red: FEM.

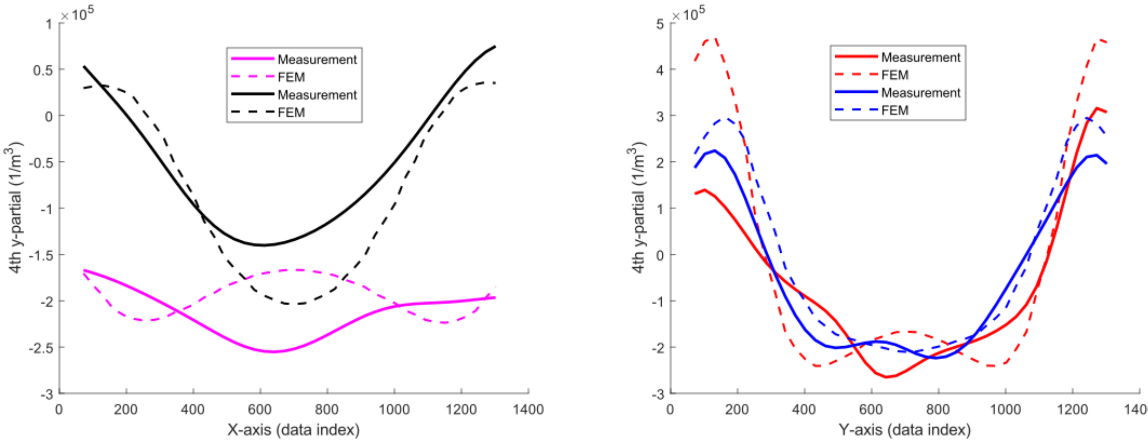

(b) Comparison in X-direction across the depicted lines.

(c) Comparison in Y-direction across the depicted lines.

Figure 10: Comparison of measured and FE-simulated deflections' 4th partial derivatives in y-direction.

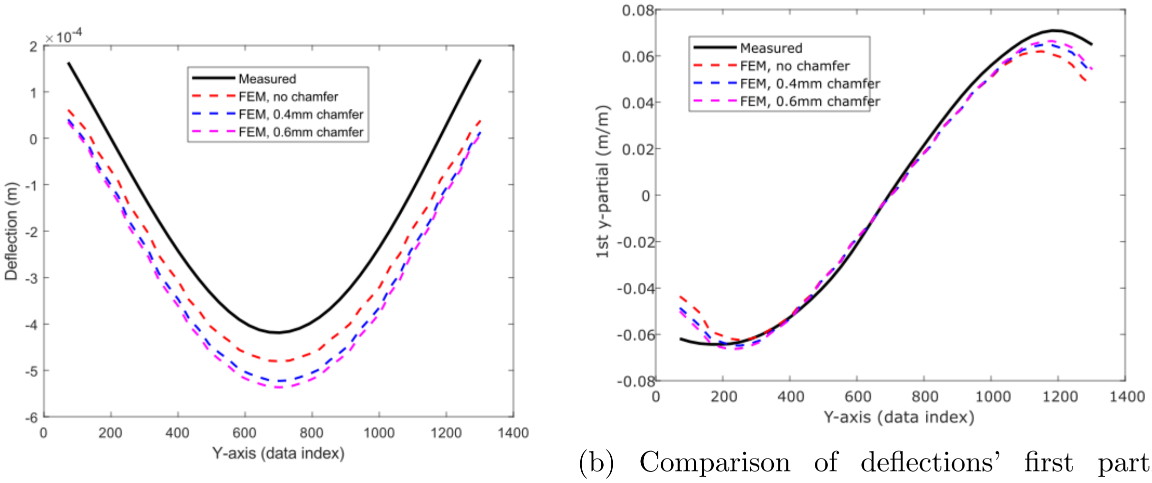

(a) Comparison of deflections.

(b) Comparison of deflections' first partial derivatives in y-direction.

Figure 11: Comparison betweem different chamfer radius values across a line in the middle of the surface in Y-direction (red line in previous Figures).

Sensitivity analysis

The accuracy of the deflection calculated from the optical measurement was compared to the change in the simulated surface shape due to changes in material constants in the FE model. The noise in the practical measurement is defined as the standard deviation in calculated surface shape between images taken under constant measurement settings comparable to the FE model. The changes in simulated surface shape due to changes in elastic modulus are the absolute values of differences between the simulated surfaces.

The practical measurement setup was as described previously. A reference image of a flat surface was captured, after which the vacuum pressure was set to 11.3 kPa. The plastic sheet was slowly moved under the camera in slight tension while continuously capturing 131 measurement images.

The deflection, $\tilde{Z}$, was calculated for all measurement images and the standard deviation of each image pixel, (x, y), between consecutive images was calculated. The resulting matrix of standard deviations was considered to describe the measurement noise. In other words, the measurement noise ϵ_m is defined as

$$\epsilon_m(x,y) = \sqrt{\frac{1}{130}\sum_{i=1}^{131}\left(\tilde{Z}_i(x,y) - \mu(x,y)\right)^2}, \quad \mu(x,y) = \frac{1}{131}\sum_{i=1}^{131}\tilde{Z}_i(x,y). \tag{16}$$

The deviation in the simulated surface,w, is defined as

$$\delta_{E,\nu}(x,y) = |w(x,y) - w_{E,\nu}(x,y)|, \tag{17}$$

where w is the simulated surface of default FE model ($E = 920\,\text{MPa}, \nu = 0.36$) describing the real material and $w_{E,\nu}$ is that of the model with deviated material constants E, ν.

The measurement noise and the simulated surface deviation when the elastic modulus is increased to 1000 MPa are depicted in Figure 12. The maximum value of the noise divided by the maximum value of deviation in surface height as a function of the elastic modulus can be seen in Figure 13.

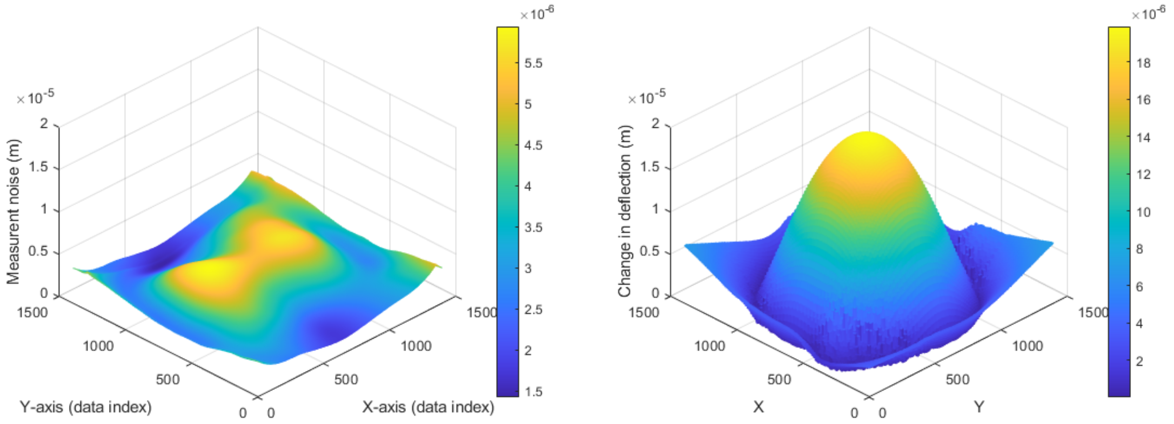

(a) Measurement noise.

(b) Deviation in simulated surfaces.

Figure 12: Comparison between measurement noise and the deviation in simulated surface when the elastic modulus in increased from 920 MPa to 1000 MPa

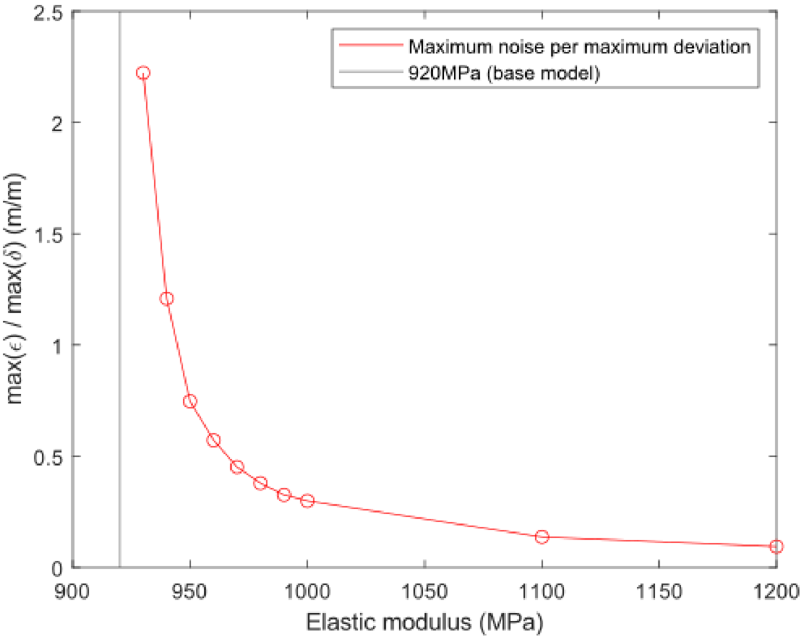

Figure 13: Maximum measurement noise per maximum deviation in FE simulated surface when elastic modulus is increased (compared to the model with elastic modulus of 920 MPa).

Discussion

The deflections depicted in Figure 7 have similar shape, however there is a clear offset DC component. This can mostly be attributed the fact that only representations of the partial derivatives are obtained in the optical measurement. These are then integrated in Fourier domain without knowledge of the constant of integration.

The first partial derivatives in Figure 8 also match well, especially near the center. There are significant differences near the contact area between the plastic sheet (or its model) and the edge of the supporting plate. This can be due to multiple factors, such as the contact model used in the FE model or the choice of chamfering. The edge chamfer was shown to affect the partials near the edge in Figure 11. The real value of the chamfer radius in the measurement system is difficult to obtain. Moreover, the chamfer may be uneven around the radius of the hole due to wear from use in the paper machine. The supporting metal plate experiences friction during measurement and the edges round out during use especially in the direction of travel of the material.

The coefficient of friction in the real measurement system was not known. For future work, tests similar to the chamfer tests could be conducted for different friction and contact models. A single test was conducted on the model with chamfer value of 0.4 mm, where the friction model was changed to ”penalty” with 0.2 coefficient of friction. The effects of this change were negligibly small.

The measurement noise naturally compounds in differentiation, which is seen as inaccuracy in the second partial derivatives in Figure 9. The general shape of the measured second partial derivative adheres to that of the simulated, but the differences are much larger and occur near the center as well. The noise becomes dominant in the fourth partial derivatives and no clear shape in the measured data can be identified compared to the FE simulated data, as seen in Figure 10.

The filtering of the derivatives has a very significant impact on the shape and magnitude of the partial derivatives, especially the higher order ones. For this reason, the fourth order partial derivatives (or the other derivatives, to less extent) depicted in Figure 10 do not represent the actual derivatives very well, but since the same filtering is done to both measured and simulated data, these are comparable. The simulated data could be differentiated with lighter filtering without much noise accumulation. The measured data quickly becomes noisy without heavy filtering to the degree that no comparison of shapes is possible.

The sensitivity analysis revealed that the standard deviation of even the surface shape between consecutive optical measurements is quite high in comparison to deviations occurring in the simulated deflections due to small changes in the elastic modulus of the material. The measurement noise defined in this analysis represents all possible sources of noise, including small surface variations and changes in the applied tension when the material is moved. Differences in the generated vacuum pressure between images is also possible. The components of noise in this analysis are also present in a realistic measurement scenario with the sensor, where their effect is likely much greater.

Conclusion

An optical measurement system for surface deflection of a plastic sheet was compared to a FE model. The measured deflection was in good agreement with the simulated deflection, however the higher order derivatives of the deflection showed discrepancies. These are likely due to the measurement noise in the optical system compounding in numerical differentiation.

Since the measurement system is developed to calculate the bending stiffness of a plate utilizing plate models that require knowledge of the fourth order partial derivatives, the compounding noise proves problematic. Moreover, sensitivity analysis showed that the sensor would have difficulties in detecting changes in surface deflection due to small changes in the elastic modulus of the material.

References

[1] J. Ackermann and M. Goesele A Survey of Photometric Stereo Techniques. *Foundations and Trends in Computer Graphics and Vision*, 9(3–4):149–254, 2015. http://dx.doi.org/10.1561/0600000065

[2] R. Allan. Concepts to maximise benefit from on-line stiffness measurement. *Appita Journal*, 68(3):211–218, 2015. https://search.informit.org/doi/10.3316/informit.366086116725586

[3] A. Chakrabarti and K. Sunkavalli. Single-Image RGB Photometric Stereo with Spatially-Varying Albedo *2016 Fourth International Conference on 3D Vision (3DV)*, 258–266, 2016. https://dx.doi.org/10.1109/3DV.2016.34

[4] L. Chase and J. Goss and L. Anderson. On-line sensor for measuring strength properties. *Tappi Journal*, 72(12):89–97, 1989.

[5] R.T. Frankot and R. Chellappa. A method for enforcing integrability in shape from shading algorithms. *IEEE Transactions on Pattern Analysis and Machine Intelligence*, 10(4):439–451, 1988. https://dx.doi.org/10.1109/34.3909

[6] P. Gutman, and B. Nilsson. Modelling and prediction of bending stiffness for paper board manufacturing. *Journal of Process Control*, 8(4):229–237, 1998. https://dx.doi.org/10.1016/S0959-1524(97)00036-X

[7] M. K. Ramasubramanian, and R.Venditti and K. Katuri. Behavior of paper on a high speed conveyor subjected to air jet impingement: a method for estimating bending stiffness. *Journal of Mechanics of Materials and Structures*, 2(2):201–219, 2007. https://dx.doi.org/10.2140/jomms.2007.2.201

[8] M. Salo and A-L. Erkkilä and M. Vilkko and M. Kanerva. Paper bending stiffness and web tension measurement from a running web using a vacuum and computer imaging. *TAPPI Journal*, 22(5):346, 2023. https://dx.doi.org/10.32964/TJ22.5.344

[9] M. Salo and J. Jokinen and M. Vilkko and M. Kanerva. Plate Bending Models for Paper Manufacturing Processes and Comparisons to Simulations with Finite Element Methods. *IFAC-PapersOnLine*, 56(2):11106–11110, 2023. https://dx.doi.org/10.1016/j.ifacol.2023.10.821

[10] M. Salo and J. Jokinen and M. Vilkko and M. Kanerva. Extension of paperboard modelling with Föppl–von Karman terms for improved stress state under suction pressure. *Rakenteiden Mekaniikka*, 57(3):80–98, 2024. https://dx.doi.org/10.23998/rm.143897

Mikko Salo, Mikko Kanerva
Tampere University
Korkeakoulunkatu 6, 33720 Tampere, Finland
`mikko.salo@tuni.fi, mikko.kanerva@tuni.fi`

Jarno Jokinen, Nazanin Pournoori, Matti Vilkko
Tampere University
Korkeakoulunkatu 6, 33720 Tampere, Finland
`jarno.jokinen@tuni.fi, matti.vilkko@tuni.fi`